PUBLICATIONS

Geophysical Research Letters

Supporting Information for

Seabed seismographs reveal duration and structure of longest runout sediment flows on Earth

Megan L. Baker[1*], Peter J. Talling[1,2], Richard Burnett[3], Ed L. Pope[1], Sean Ruffell[2], Morelia Urlaub[4], Michael A. Clare[5], Jennifer Jenkins[2], Michael Dietze[6,7], Jeffrey Neasham[3], Ricardo Silva Jacinto[8], Sophie Hage[9], Martin Hasenhündl[10,11], Steve M. Simmons[12], Catharina J. Heerema[2,13], Maarten S. Heijnen[5,14], Pascal Kunath[4], Matthieu J. B. Cartigny[1], Claire McGhee[15], Daniel R. Parsons[16]

[1]Department of Geography, Durham University; South Road, Durham, DH1 3LE, UK.

[2]Department of Earth Sciences, Durham University; South Road, Durham, DH1 3LE, UK.

[3]School of Engineering, Newcastle University; Newcastle upon Tyne, NE1 7RU, UK.

[4]GEOMAR Helmholtz Centre for Ocean Research; Wischhofstraße 1-3, 24148 Kiel, Germany.

[5]National Oceanography Centre; Southampton, SO14 3ZH, UK.

[6]Department of Geography, Georg-August-University; Goldschmidtstr.3, D-37077 Göttingen, Germany.

[7]Section 4.6 Geomorphology, Deutsches GeoForschungsZentrum GFZ Potsdam; Telegrafenberg F427, D-14473 Potsdam, Germany.

[8]Geo-OceanUnit, IFREMER Centre de Brest; Plouzané, France.

[9] GEOPS, UMR 8148, Université Paris-Saclay; France

[10] Institute of Hydraulic Engineering and Water Resources Management, TU Wien; 1040 Vienna, Austria.

[11]Institute for Hydraulic Engineering and Hydrometry, Federal Agency for Water Management; 1200 Vienna, Austria

[12]Energy and Environment Institute, University of Hull; HU6 7RX, UK.

[13]Expert Analytics; Møllergata 8, 0179, Oslo.

[14]School of Ocean and Earth Sciences, University of Southampton; European Way, Southampton SO14 3ZH, UK.

[15]School of Natural and Environmental Sciences, Newcastle University; Newcastle upon Tyne NE1 7RU, UK.

[16]The Loughborough Centre for Sustainable Transitions: Energy, Environment and Resilience, Loughborough University; Leicestershire, LE11 3TU, UK.

Contents of this file

Introduction

The supporting information in this document includes (1) Supplemental Materials and Methods, (2) supporting Figures S1 to S12, and (3) supporting tables S1 to S2.

Text S1. Supplemental Materials and Methods

Field deployment of ADCP moorings and OBSs

Twelve ocean-bottom seismographs (OBSs) and eleven moorings with acoustic Doppler current profilers (ADCPs) were deployed along the Submarine Congo Canyon-Channel over a four-week period between 9th September 2019 to 2nd October 2019, divided into canyon and channel subarrays (Figure 1). The 75, 300 and 600 kHz ADCPs were suspended 44-250 m above the canyon floor from a fixed mooring anchored within the canyon-channel. The OBSs were deployed 0.7 to 2.9 km away from the centre of the canyon-channel, on flat canyon terraces or on overbank areas outside the channel. The location of each OBS is based on the ship's position when the instrument was deployed, whilst the location of each ADCP mooring was confirmed to within +/- ~15 m by ultra-short baseline acoustic positioning. OBS drift while sinking is expected to be small, as there were minimal ocean currents and triangulation of the ADCP moorings showed instruments drifted an average of 54 m from ship's position at deployment. Two ADCP moorings surfaced in October 2019 and another in December 2019, while the remaining eight were broken by the 14-16th January 2020 turbidity current event (Flow 10). Emergency ship charters were used to recover nine of eleven ADCP-moorings drifting on the ocean surface, which was especially challenging as it occurred during the Covid-19 pandemic (Talling et al., 2022). The OBSs were not damaged by the >1,000 km runout, canyon-flushing flows and recorded ~8-10 months of data, depending on battery life. Ten of the twelve OBS instruments were recovered, with the two unrecovered instruments unresponsive during retrieval, suggesting they may have been damaged or buried under sediment during the deployment period. Figure 1 only shows the locations of the ADCPs and OBSs used in the analysis.

OBS data

OBS1 to OBS8 consisted of three-channel Sercel L28-LB geophones and a Hi-Tech HTI-90U hydrophone. The most distal seismic station (OBS9), located 1071 km offshore, contained a three-channel Owen (4.5 Hz) Geophone and a Hi-Tech HTI-04 hydrophone. The geophone and hydrophone output was sampled at a frequency of 1 kHz. The most distal OBS9 station also contained a thermometer located on the frame, which logged the temperature every minute for the 10-month deployment period to a resolution of 0.01 °C.

Seismic data processing

The instrument response was removed from the vertical component of the OBS data to enable analysis of low-frequency signals below 4.5 Hz. The data was converted from raw counts to units of velocity (m s^{-1}) and corrected to account for the instrument response using the open-source Python framework ObsPy (Beyreuther et al., 2010). Data were first down sampled by a factor of 10 to give a sample rate of 100 Hz (Nyquist frequency of 50 Hz). This was done to minimise data processing times, and as initial data inspection indicated no relevant signals >50 Hz. Data were pre-filtered by applying a band-pass filter between 0.2 and 50 Hz. After the instrument response was removed, data were further filtered with a 1 Hz highpass filter to remove the noisy low frequency data that was amplified by the instrument response correction. Spectrograms were generated using fast Fourier transform, with a Hanning window of 20 s and a 50% overlap. Spectrograms show spectral power of seismic signals through time at different frequencies, where frequency is defined as the number of seismic waves from the signal that pass the geophone in one second. The spectrograms results are given in decibels (dB) relative to velocity ($10\log_{10}[(m/s)^2/Hz]$).

The hydrophone data was explored by plotting spectrograms of the raw data using a fast Fourier transform with a Hanning window of 20 s and a 50% overlap. The spectrograms showed that the hydrophones did not record any turbidity current acoustic signals (supporting information Figures S6 and S7), confirming that the geophone recorded ground-bound seismic signals generated by the turbidity currents.

Identification, transit velocity, and characterisation of turbidity current pulses

The start of a turbidity current event was manually picked from the exponential curve of the seismic data (expressed in counts), when the signal exceeded a threshold of 10% above background whilst the end of the event was picked when the seismic signal returned to 10% below background, pre-event values. The errors introduced in transit velocity and pulse durations from manually picking the start and end of the event were ~0.1 m s^{-1} and ~120 s, respectively.

The front-to-back length of the pulse was estimated by multiplying the transit velocity of the pulse by the duration of the pulse at each station (supporting information Table S1). This front-to-back length was also verified by determining the spacing of OBS sites that recorded a seismic signal at the same moment in time. To determine the front-to-back length of the pulse at OBS1, which has no velocity measurements, the transit velocity at nearest adjacent OBS (OBS2) was used. We note that transit velocities appear to initially accelerate within the canyon, such that the transit velocity at OBS1 is likely to be less than at OBS2, thus estimates of front-to-back length of the pulse at OBS1 are likely to represent the upper-end of true front-to-back pulse length. Pulse duration and front-to-back pulse length are calculated values of the flow frontal-cell behaviour based on the seismic signal. If anything, they are likely to be an overestimate, as the OBSs record the flow not as it directly passes them, but earlier when it is an estimated straight-line distance of 1.1 to 5.7 km away (see *Comparison of turbidity current arrival time between ADCP moorings and OBSs*). Furthermore, the measurements have not been corrected for the different seabed conditions and coupling responses at each OBS. However, these values provide a general trend of turbidity current pulse behaviour through the system.

Consideration of ground response

A source signal received by seismic sensors will have been modified due to geometric spreading, inelastic attenuation, and local characteristics of the ground through which the seismic waves have travelled (site effects), which is collectively described as the *ground response* (Cook & Dietze, 2022). As such, the waveform characteristics of the seismic signal recorded by each OBS should not be directly compared, as we do not know how subsurface structure, canyon geometry and distance of OBS from turbidity current source will modify the seismic signal received.

To account for differing ground responses at each OBS station, the seismic signal of turbidity current events throughout the deployment period are only compared for single stations. When a turbidity current is tracked through the canyon and channel subarrays and the signal is measured between OBSs, only general trends (e.g., arrival times) in seismic pulse signature observed across multiple stations are presented and discussed.

Calibrating turbidity current seismic signals using ADCP-mooring data

Turbidity currents recorded by OBS3 are compared to the velocity data from the adjacent M2 mooring (Figure 2), which contained a 75 kHz ADCP located in the canyon 250 m above the seabed (Figure 1E). The ADCP on M2 recorded a vertical velocity profile every 45 s, which consisted of 43 individual measurements with a vertical spacing of 6 m. Each velocity measurement measured the velocity in x, y, and z orientation. For each ADCP profile, the square root of the sum of the individual velocity components squared was calculated to determine the velocity magnitude. The maximum velocity magnitude from each profile was then extracted to produce a time series, which could be compared with the time series of the raw seismic data (in counts) recorded by OBS3 (averaged over a 45 second window). For the four turbidity currents where the seismic signal and velocity data can be compared, only the fast front of the flow travelling at >1.6 m s^{-1} produces a discernible seismic signal (Figure 2 and supporting information Figure S4). Two smaller flows with maximum velocities of 0.57 m s^{-1} and 0.67 m s^{-1} identified in the ADCP data did not produce observable signals in OBS spectrograms. However, we note that observability is likely to vary with OBS distance to canyon-channel, as well as site coupling, ground response, and background noise levels.

Depth-averaged flow concentrations from ADCP-mooring data

Depth-averaged sediment concentrations from the directly measured flow velocity and flow height (via the ADCP-mooring) were determined using iteratively solved modified Chézy equations following the approach of Pope *et al.* (2022) for Flow 1 (supporting information Figure S8). Applied here to turbidity current flows, the Chézy approach is typically used in river studies to calculate open channel flow characteristics by balancing the driving and frictional forces. This method gives a single depth-averaged concentration for each flow velocity profile. In reality, concentration varies with height in the flow, and is likely to be higher closer to the bed (Pope et al., 2022).

The highest resolution 600 kHz ADCP mooring (ADCP M3) was selected for this analysis to enable the most accurate calculations. The ADCP on M3 recorded a velocity profile every 11 s, consisting of 53 individual measurements with a vertical spacing of 0.75 m. This mooring was located 55 km downstream of the 75 kHz ADCP (ADCP M2) which was adjacent to OBS3 and used to calibrate the seismic signals. Strong similarities in the observed velocity structure of flows recorded by ADCP M2 and ADCP M3, allow for the depth-averaged flow concentration findings derived from the ADCP M3 to be applied to the flow further upstream.

For this analysis, the depth-averaged flow velocities (U) and flow height (H) were first calculated from the ADCP M3 velocity data. For flow height, the seabed reflector was often obscured during the passage of the front of the faster flows. For these situations, the base of the flow was defined as the deepest received velocity measurement. Since the base of the flow is likely to be below this value (by ~ 5 m), the actual flow front height would have been higher than used in the Chézy calculations. Thus, the depth-averaged velocities likely underestimated the true depth-averaged velocity of the fast flow fronts, and the depth-average sediment concentration from these parts of the flow are likely to be greater than the predicted concentrations calculated with this method.

The depth-averaged sediment concentration (C) was calculated using equation 1:

$$U^2 = \frac{1}{C_{fi} + C_{fb}} RCgHS \quad (1)$$

where R is the submerged specific gravity of the sediment, taken here to be the value for quartz (~1650 kg m^3), g is the gravitational acceleration (9.81 m s^{-2}), and S is the slope gradient at the mooring calculated from the bathymetry (0.34°). C_{fb} is the bottom friction coefficient of 0.002. The friction on the top interface of the fluid (C_{fi}) is calculated using equation 2:

$$C_{fi} = \frac{0.0075}{\sqrt{1 + 718Ri^{2.4}}} (1 + 0.5Ri) \quad (2)$$

where the bulk Richardson number (*Ri;* i.e. the amount of turbulence) is determined following Parker *et al.* (1987):

$$Ri = \frac{RgCH}{U^2} \quad (3)$$

Organic carbon flux calculations

Baker *et al.* (2024) calculated that the two canyon-flushing turbidity currents eroded 43 ± 15 Mt of terrestrial organic carbon along the length of the Congo Canyon-Channel. The eroded organic carbon mass from Baker *et al.* (2024) can be combined with the new information on flow duration to estimate for the flux per unit time of organic carbon to the deep-sea by canyon-flushing turbidity currents. This assumes that most of the eroded sediment and organic carbon was contained in the frontal-cells of the canyon-flushing flows. This is a reasonable assumption as frontal-cells have been shown to dominate sediment fluxes in flows elsewhere (Pope et al., 2022; Simmons et al., 2020). For example, measurements of turbidity currents in Bute Inlet, Canada, demonstrated that frontal-cells can transport up to 1000 times more sediment than the dilute body and thus dominate turbidity current sediment fluxes (Pope et al., 2022). Furthermore, given the fast speed of the canyon-flushing flows at the distal OBS (between 4.6 m s^{-1} to 7.6 m s^{-1}), it is reasonable to assume that the majority of the eroded sediment was flushed beyond the channel mouth and onto the lobe. This is supported by the lack of deposition observed in the channel in the time-lapse bathymetric surveys (Ruffell et al., 2024; Talling et al., 2022). Thus, the 43 ± 15 Mt of organic carbon was mainly flushed to the deep-sea in ~23 hours, the combined duration of the canyon-flushing frontal-cells (supporting information Table S1).

Comparison of turbidity current arrival time between ADCP moorings and OBSs

For the six occurrences where the timing of turbidity current arrival at an ADCP mooring and adjacent OBS can be compared, the OBSs always recorded the turbidity current arrival before the ADCP moorings in the order of minutes. This is despite the ADCP moorings being in the direct flow path of the turbidity currents, while the OBS stations relevant for this analysis were located 700-1200 m away from the centre of the canyon-channel (Figure 1). This suggests OBSs successfully recorded ground motion generated by turbidity currents from a distance. To estimate the distance from which each OBS could detect turbidity current events travelling down the canyon-channel, the time difference between the turbidity current arrival recorded at an ADCP mooring and the adjacent OBS was multiplied by the maximum ADCP flow velocity (or the transit velocity for Pulse 10A of Flow 10). As the speed of seismic waves is 2-3 orders of magnitude faster than the turbidity current flow velocities, the travel time for the seismic waves to reach the OBS are considered negligible (<< 1 s) in these calculations.

The time delay between ADCP mooring and OBS turbidity current arrival times ranged from ~4.5-37 minutes (supporting information Table S2). This suggests that the OBSs start to receive turbidity current seismic signals when the flow is a straight-line distance of 1.1 to 5.7 km away (supporting information Table S2). There is no correlation between turbidity current velocity and the time delay between the ADCP and OBS arrival times across all arrival time comparisons, including the four examples utilising OBS3 where the ground response is constant. However, a wide range of distances may be expected due to a range of flow behaviours which may influence the seismic signal generated, such as sediment concentration and average sediment grain-size (Burtin et al., 2016).

Transit speed of pulse 10A from ADCP data and timings of cable breaks

The transit speed of Pulse 10A was also calculated using the ADCP moorings, by dividing the distance between adjacent ADCP mooring locations with the difference in arrival time (supporting information Figure S12). This transit speed calculation also utilised the timing of the SAT3 and WACS cable breakages, which are known to the nearest minute. This assumes that the cable is immediately broken by the arrival of the flow. This assumption is reasonable based on the timings of the breakages; the WACs cable broke at 07.54 am on 16th January, 45 minutes before the arrival of the Pulse 10A was recorded at OBS5 (08.39 am), 25 km further along the canyon. These arrival times and distances give a transit velocity of ~9 m s^{-1} between WACS cable and OBS5, this is similar to the 7.6 m s^{-1} transit velocity recorded between OBS5 and OBS6. To get a transit speed of 7.6 m s^{-1}, the cable breakage would need to have occurred at 08.03 am, i.e., within 10 minutes of arrival of the flow front at the cable.

Supporting information Figures S1 to S12

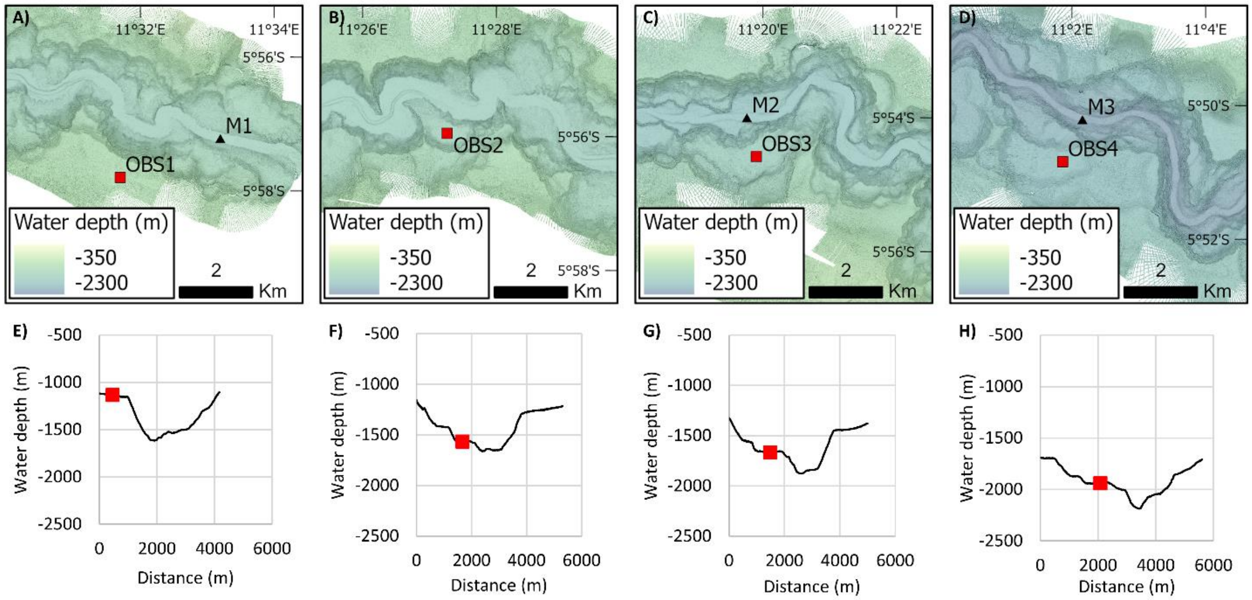

Figure S1. Locations of OBSs and adjacent ADCP moorings deployed in the Congo Canyon**.** (a to d) Bathymetric maps show the locations of OBSs (red squares) situated outside the canyon, and adjacent ADCP moorings (black triangles) located in the canyon. (e to h) Bathymetric cross sections (from south to north) showing the position of each OBS relative to the canyon profile.

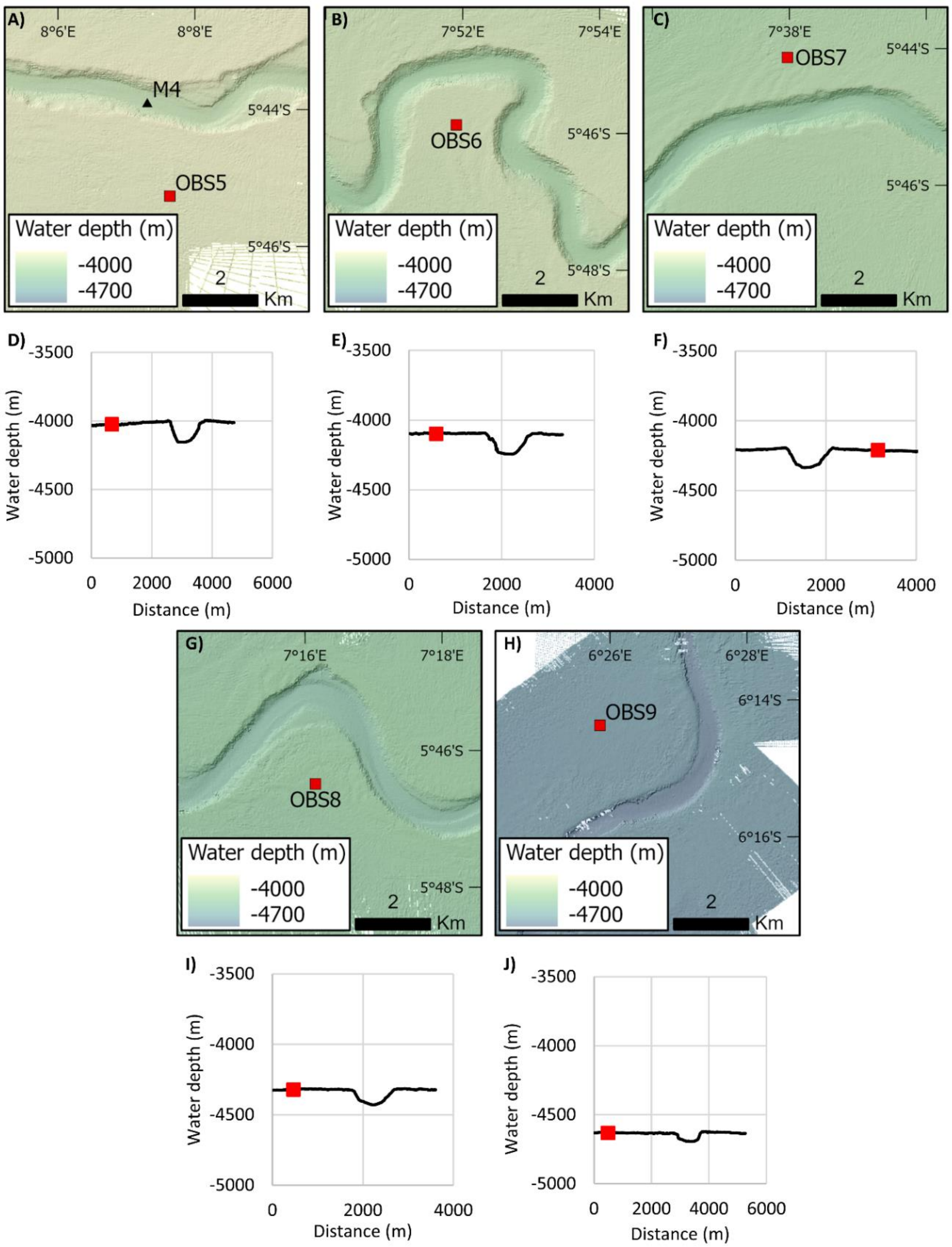

Figure S2. Locations of OBSs and adjacent ADCP moorings deployed in deeper-water Congo Channel. (a to c and g to h) Bathymetric maps show the locations of OBSs (red squares) situated outside the channel, and adjacent ADCP moorings (black triangles) located in the channel. (d to f and i to j) Bathymetric cross sections (from south to north) showing the position of each OBS relative to the channel profile.

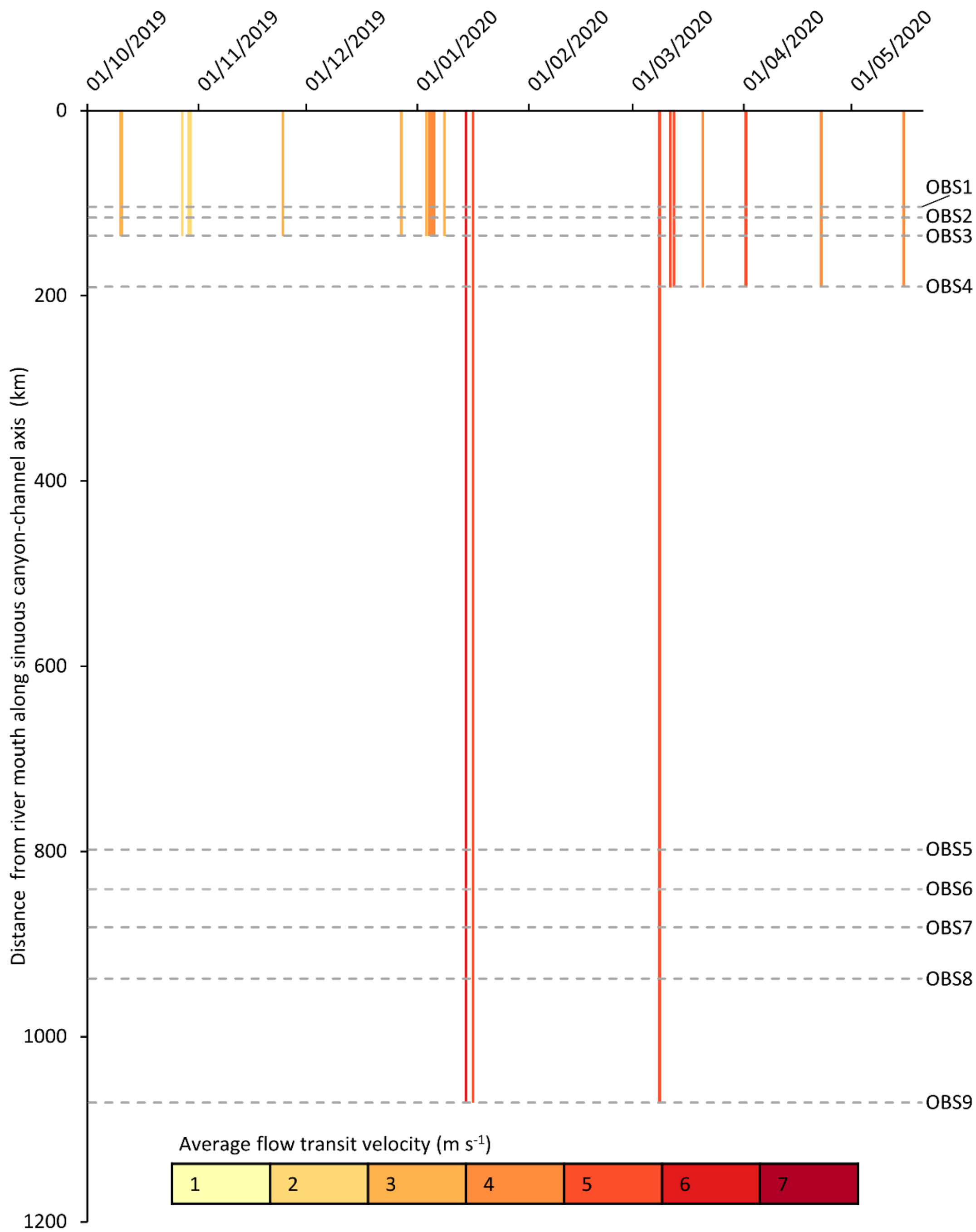

Figure S3. Timing and runout distance of turbidity current pulses recorded by OBS in the Congo Canyon-Channel between October 2019 and May 2020. Pulses have an average recurrence interval of 14 days, but there is no obvious clustering of events.

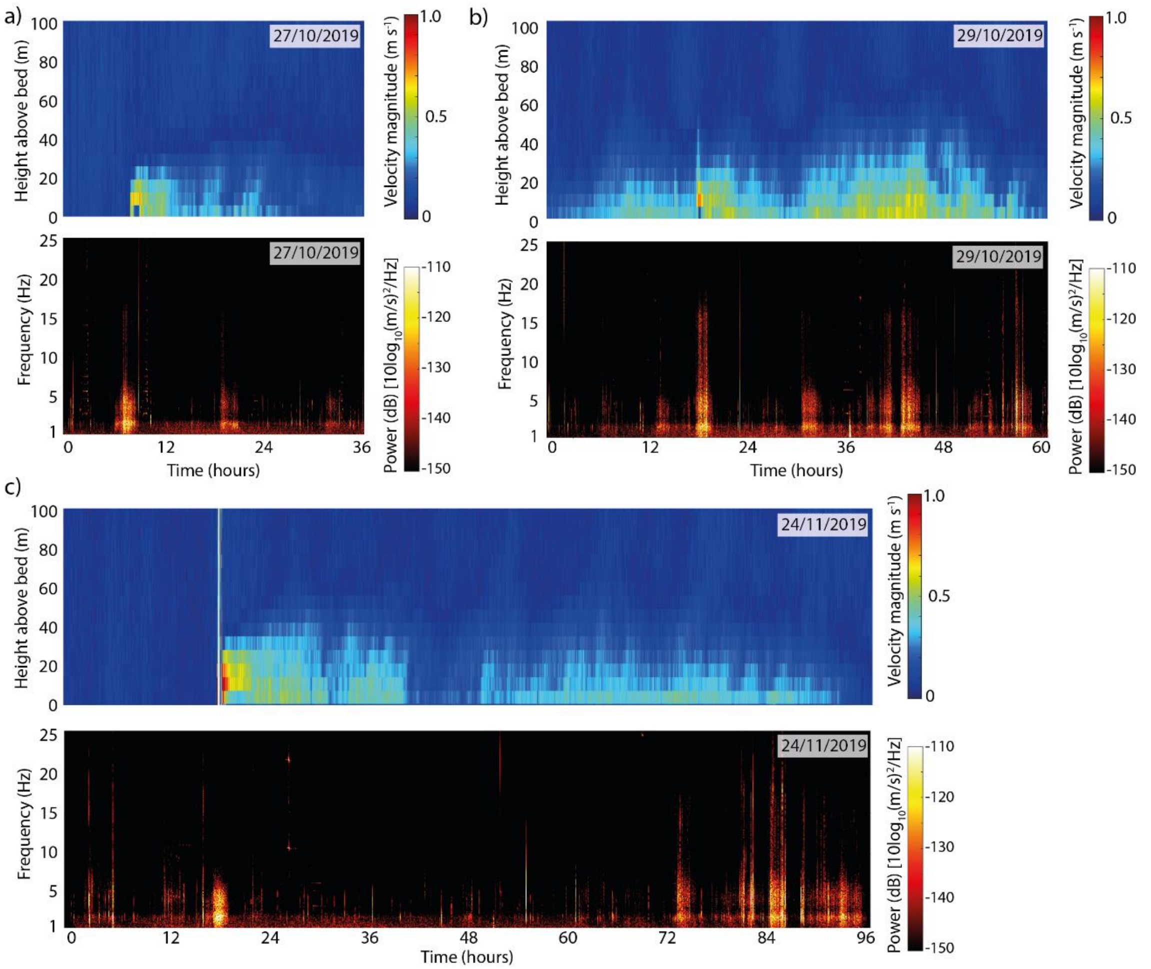

Figure S4: Mooring M2 ADCP time series of turbidity current velocity profiles and OBS3 spectrograms below showing intensity of seismic signals during the turbidity current event for a) Flow 2, b) Flow 3 and c) Flow 4.

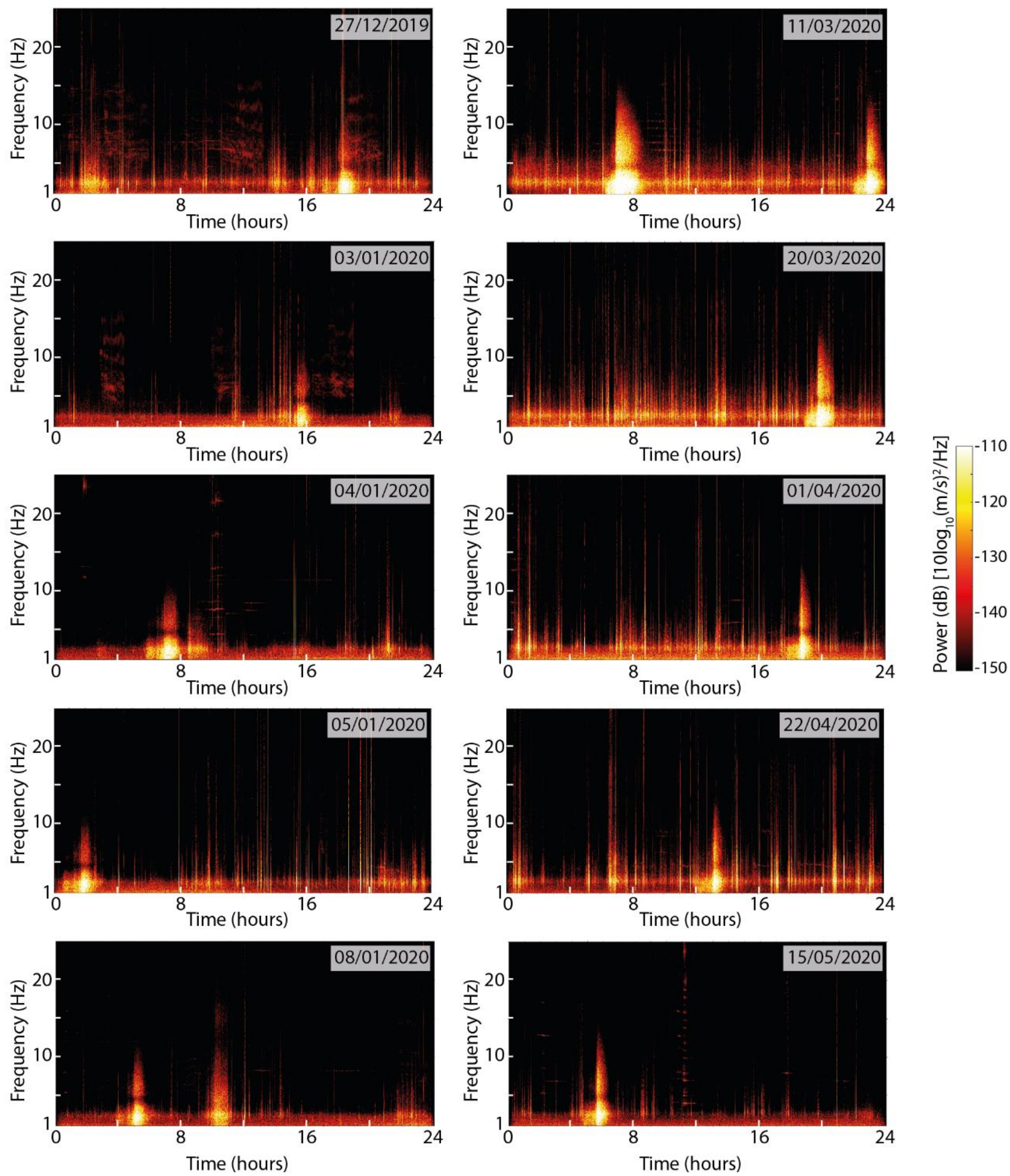

Figure S5: Spectrograms showing intensity of seismic signals during turbidity current events recorded by OBS 3 for Flows 5 to 9 and Flows 12 to 16 (for Flows 10 and 11 see Figure 2).

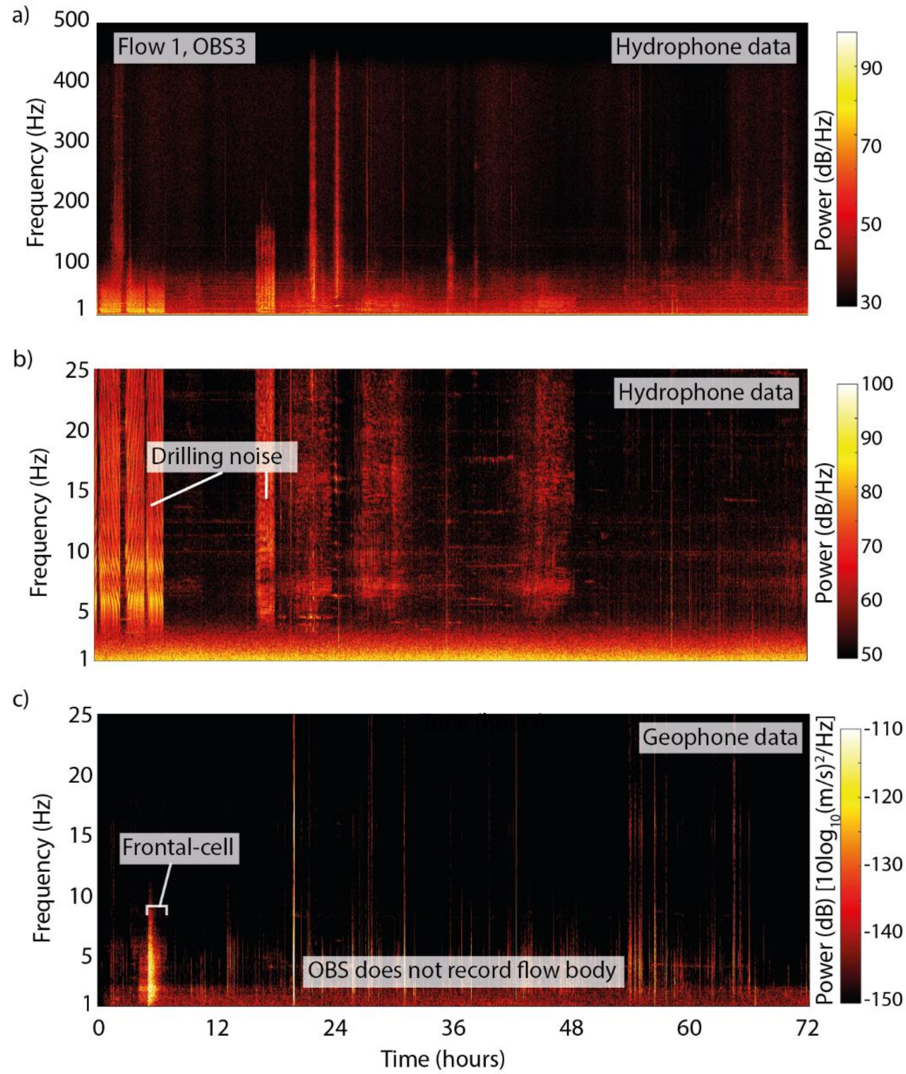

Figure S6: Comparison of turbidity current signals recorded by the hydrophone and geophone on OBS 3 for Flow 1. (a) Hydrophone spectrogram across the full frequency range and (b) hydrophone spectrogram across the 1-25 Hz frequency range show that the hydrophone did not receive any acoustic signals from the turbidity current. (c) Geophone spectrogram showing the seismic signals received from the turbidity current.

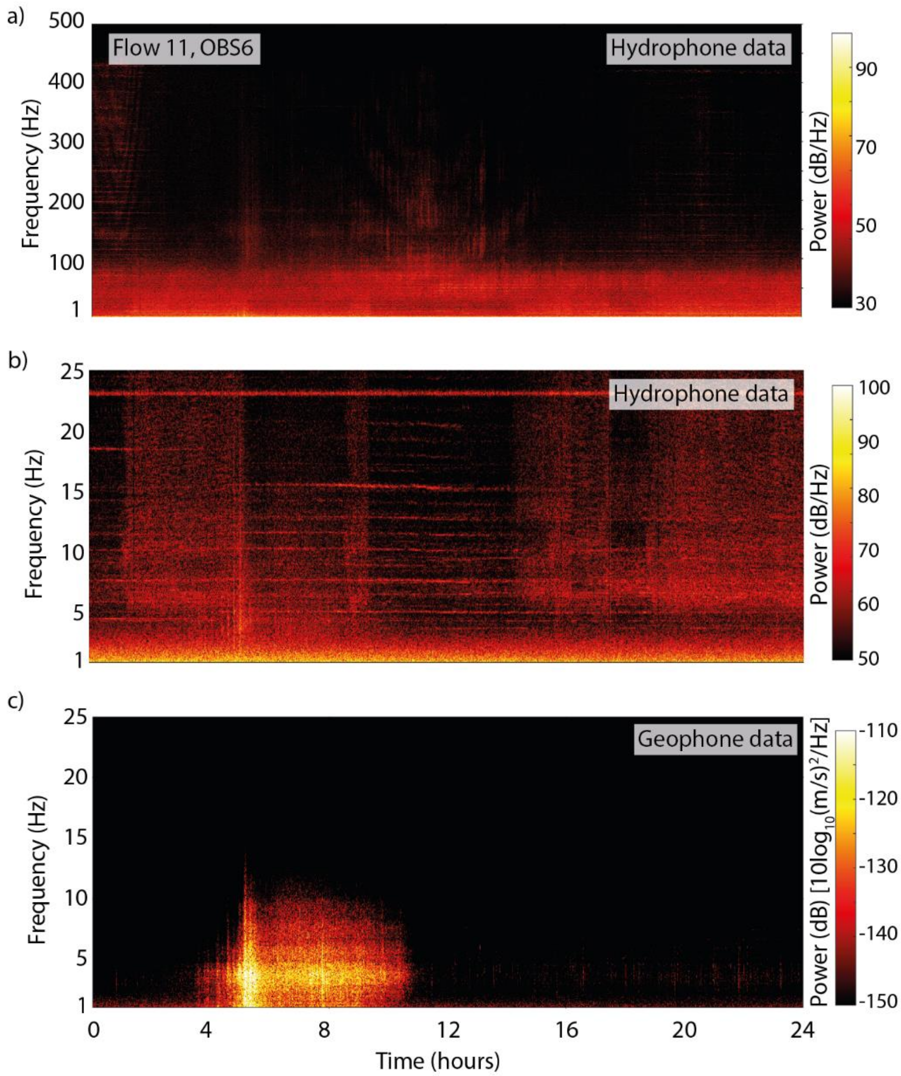

Figure S7: Comparison of turbidity current signals recorded by the hydrophone and geophone on OBS6 for Flow 11. (a) Hydrophone spectrogram across the full frequency range and (b) hydrophone spectrogram across the 1-25 Hz frequency range show that the hydrophone did not receive any acoustic signals from the turbidity current. (c) Geophone spectrogram showing the seismic signals received from the turbidity current.

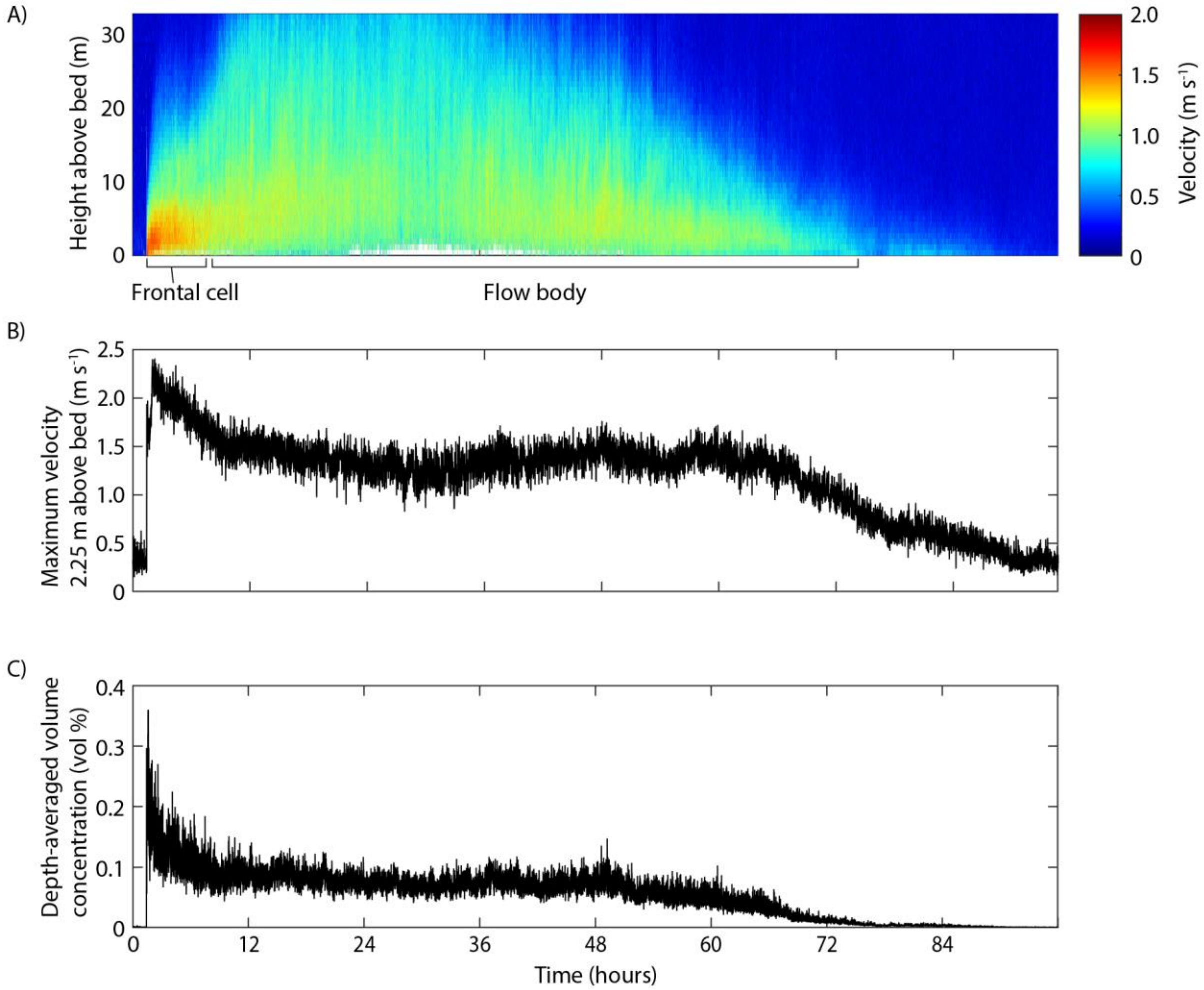

Figure S8. Flow velocity structure and concentration from 600 kHz-ADCP M3 data for Flow 1 on 10th October. (a) Time series of turbidity current velocity profiles showing fast moving frontal-cell, and slower trailing body. (b) Plot of maximum velocity magnitude at a height of 2.25 m above the bed. (c) Depth averaged flow volume concentration calculated using the Chézy-approach, showing how the frontal-cell is the densest part of the flow.

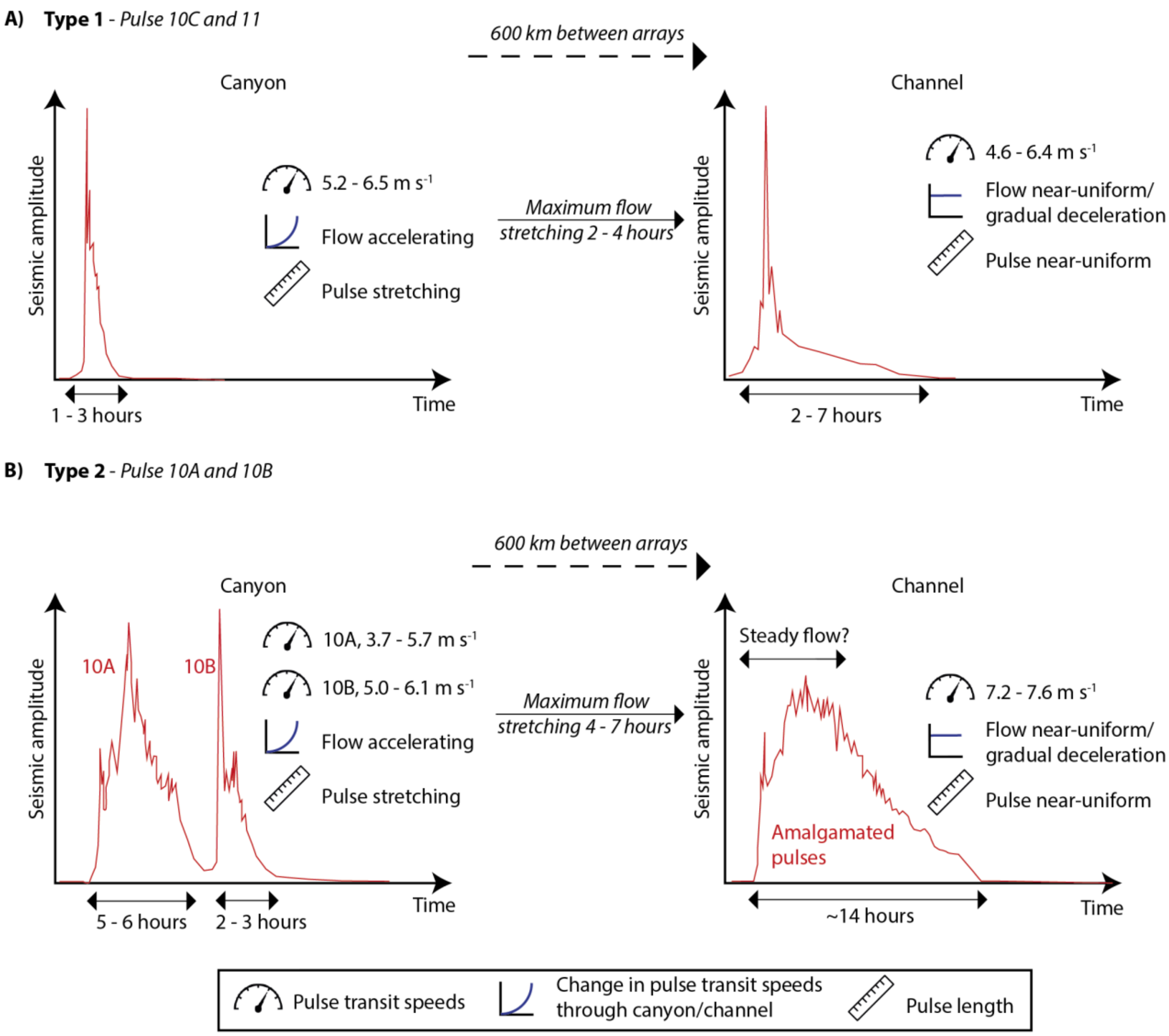

Figure S9. Summary of how seismic pulses change with distance for canyon-flushing Flows 10 and 11. (a) Type 1 pulses include pulse 10C and 11. These type 1 pulses accelerate within the canyon, but then have near-uniform pulse duration and length in the channel with gradual deceleration. (b) Type 2 pulses include pulse 10A and 10B, which were close together and amalgamated in the canyon to form a single pulse in the deep-water channel (Figure 3). In the channel, the front-to-back length and duration of both types of pulses remained near-uniform.

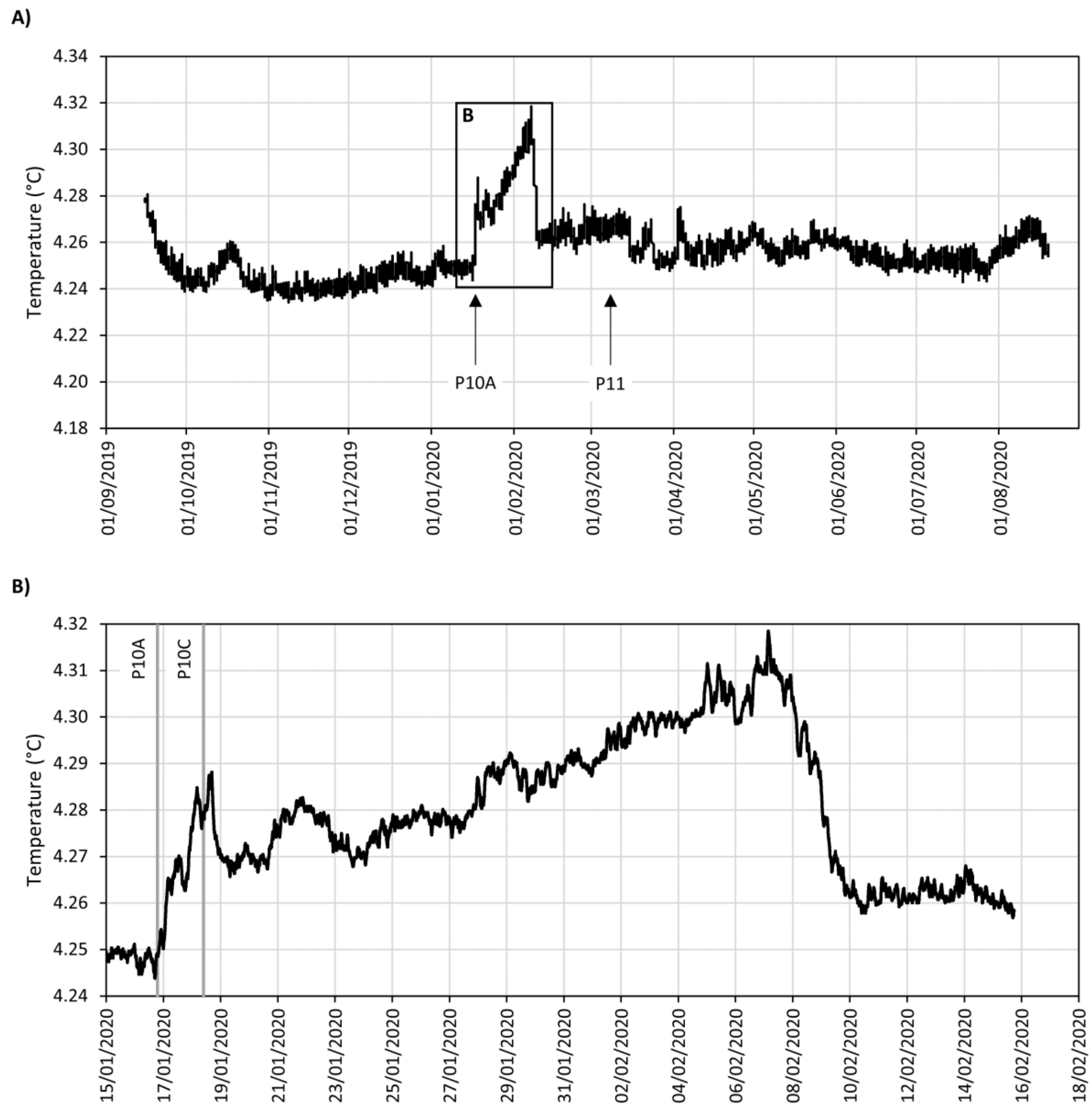

Figure S10. Temperature data from OBS9 located 1,071 km offshore at the distal end of the Congo Channel. See Figure 1 for a map of its location. (a) Temperature data for the whole OBS9 deployment period, with the timing of >1,000 km runout turbidity currents Flow 10 and 11 shown by black arrows and pulses labelled P10A and P11. (b) Plot showing that a temperature anomaly corresponds to when Pulse 10A reached OBS9 on 16th January 2020 and Pulse 10C on 18th January 2020 (vertical grey lines). Temperature remained elevated for 21 days before dropping rapidly. Temperature data did not change at OBS9 upon arrival of Flow 11, which suggests this flow may have been confined in the channel with limited overspill.

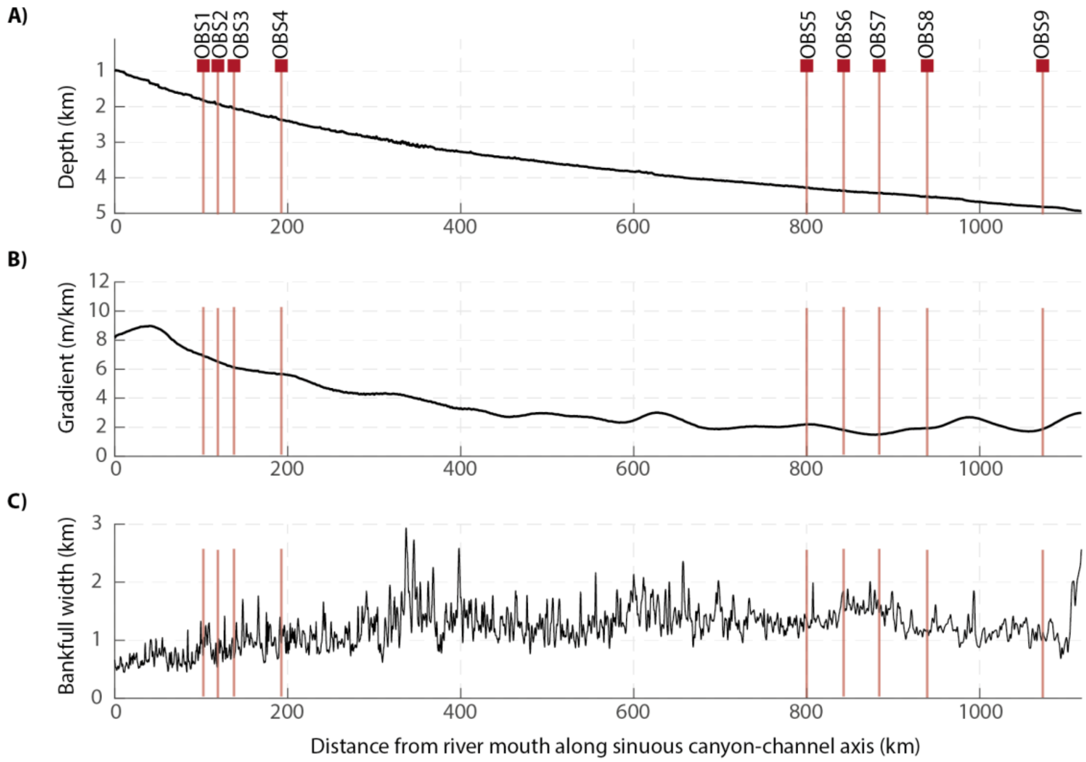

Figure S11. Changes in Congo Canyon-Channel long profile, gradient and bankfull width with distance. (a) Changes in water depth and (b) seafloor gradient with distance along the floor of the canyon-channel. (c) Changes in canyon-channel bankfull width with distance measured at crests of confining levees or first terrace.

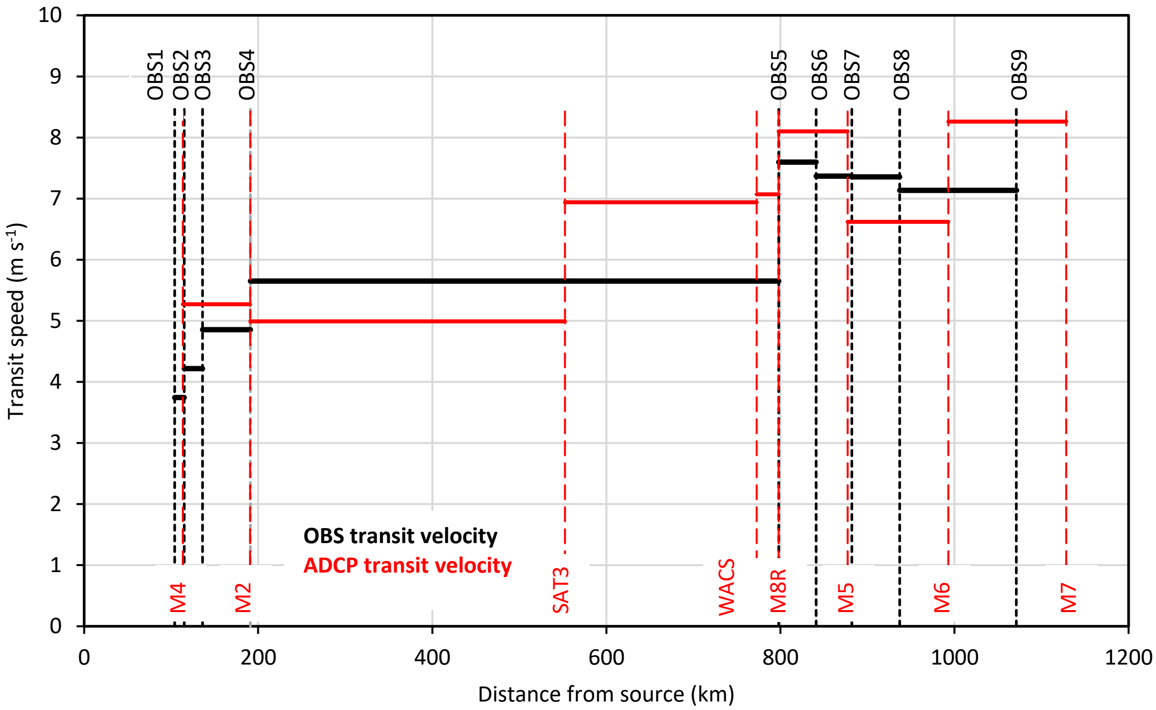

Figure S12. Comparison of transit speed of pulse 10A recorded by ADCP moorings (red) and OBSs (black). The transit speed of Pulse 10A was calculated by dividing the distance between adjacent ADCP mooring or OBS locations with difference in arrival time. The ADCPs only recorded the arrival of Pulse 10A before the anchored mooring lines were broken by the flow. The transit speed of the Pulse 10A from the ADCP moorings, also utilised the timing of the SAT3 and WACS cable breakages. M = ADCP mooring, OBS = ocean-bottom seismograph.

Supporting information Tables S1 to S2

Pulse	1	2	3	4	5	6	7A	7B	8	9	10A	10B	10C	11	12A	12B	13	14	15	16
Date	10/10/19	27/10/19	29/10/19	24/11/19	27/12/19	03/01/20	04/01/20	04/01/20	05/01/20	08/01/20	14/01/20	14/01/20	16/01/20	08/03/20	11/03/20	11/03/20	20/03/20	01/04/20	22/04/20	15/05/20
Transit velocities (m s^{-1})																				
1																				
2	2.5	3.0	1.9	2.7	2.9	3.0	2.7	3.6	3.5	3.2	3.7	5.2	5.6	5.9	4.8	4.1	5.1	4.1	3.7	4.0
3	4.0	3.4	1.7	3.7	3.3	3.3		3.6	3.6	3.5	4.2	5.0	5.2	5.2	5.1	4.0	4.1	3.5	3.4	3.7
4											4.9	6.1	6.0	6.5	6.1	5.2	5.0	3.9	3.6	4.9
5											5.7		6.4	5.7						
6											7.6		6.2	5.2						
7											7.4		5.9	5.1						
8											7.4		5.6	4.8						
9											7.2		5.1	4.6						
Pulse duration (hours)																				
1	1.7	0.9	1.1	1.0	0.4	0.6	0.6	0.7	0.7	0.6	5.8	2.3	1.1	2.1	1.0	0.6	0.6	0.8	0.6	0.7
2	1.7	1.1	1.0	1.2	1.1	0.9	0.7	1.1	0.9	0.9	6.2	2.4	1.6	3.4	1.7	0.8	1.3	1.3	1.1	1.3
3	1.0	1.6	1.9	1.7	0.9	0.7		0.9	0.7	0.7	5.5	2.8	1.9	2.9	1.3	0.6	1.0	0.6	0.6	0.7
4											5.6	2.7	1.9	2.3	1.4	0.7	1.3	0.3	0.4	1.8
5											13.4		5.6	2.0						
6											14.6		6.6	4.2						
7											14.1		6.3	3.4						
8											14.7		6.0	2.6						
9											14.0		4.6	4.8						
Pulse front-to-back length (km)																				
1	15	9	7	9	4	7	6	9	9	7	78	43	23	45	18	9	11	11	9	11
2	15	12	7	11	11	9	7	14	12	10	83	44	33	72	29	12	25	19	15	18
3	14	20	12	23	10	8		12	9	9	84	51	36	54	24	9	15	7	7	10
4											97	58	41	54	30	14	24	4	5	32
5											274		129	41						
6											399		147	78						
7											373		133	63						
8											390		122	45						
9											365		84	80						

Table S1. Transit velocity, pulse duration, and front-to-back pulse length for each turbidity current pulse recorded by OBSs**.** Flow pulses are labelled 1 to 16 and letters indicate pulse within the same flow event. Numbers 1 to 9 indicated the OBSs from proximal to distal, stations 1 to 4 are located in the canyon subarray and 5 to 9 are located in the channel subarray. Pulse front-to-back length was calculated by multiplying the pulse transit velocity by its pulse duration.

Turbidity current event	OBS station	ADCP mooring	Flow arrival at ADCP (UTC)	Flow arrival at OBS (UTC)	Time delay between ADCP and OBS flow arrival (s)	Maximum flow velocity at ADCP (m s^{-1})	Estimated distance from which OBS recorded turbidity current (m)
10/10/19	3	2	05:04:30	04:59:44	286	3.9	1115
27/10/19	3	2	14:40:30	14:03:20	2230	1.6	3568
24/11/19	3	2	18:05:15	17:38:20	1615	3.5	5653
27/12/19	3	2	18:15:00	17:57:00	1080	3.4	3672
14/01/20, P1	5	4	02:56:42	02:47:00	582	4.9	2852
14/01/20, P1	7	5	08:53:24	08:39:09	915	5.7	5206

Table S2. Time delay between turbidity currents recorded at OBSs and adjacent ADCP-moorings. OBSs recorded the arrival of turbidity currents before adjacent ADCPs. This is because the OBSs can record signals from a distance, whilst ADCPs record flows travelling directly below them. By calculating the time delay between the flow arriving at the OBS and the ADCP, and multiplying this by the maximum ADCP flow velocity (or the transit velocity for Pulse 10A of Flow 10), the distance from which the OBS can record turbidity current signals can be estimated. There is no relationship between the maximum flow velocity and the estimated distance from which OBS recorded the turbidity currents. Only a limited number of flows can be compared between the OBSs and adjacent ADCP-moorings, as some ADCP-moorings were broken in October-December 2019 by turbidity currents, and all the remaining ADCP-moorings were broken by the 14-16th January 2020 canyon-flushing turbidity current (Talling et al., 2022).